

Article

Not peer-reviewed version

Harnessing Nitrous Oxide for Sustainable Methane Activation: A Computational Exploration of CNC-Ligated Iron Catalysts

[Bruce Morland Prince](#) *

Posted Date: 22 January 2025

doi: 10.20944/preprints202501.1588.v1

Keywords: iron-oxo; iron-oxyl; oxo-cation; methane carbon-hydrogen activation; radical; oxygen radical rebound; methanol; oxo; oxyl; hydrogen atom abstraction; HAA; hydrogen atom transfer; HAT; intersystem



Preprints.org is a free multidisciplinary platform providing preprint service that is dedicated to making early versions of research outputs permanently available and citable. Preprints posted at Preprints.org appear in Web of Science, Crossref, Google Scholar, Scilit, Europe PMC.

Copyright: This open access article is published under a Creative Commons CC BY 4.0 license, which permit the free download, distribution, and reuse, provided that the author and preprint are cited in any reuse.

Article

Harnessing Nitrous Oxide for Sustainable Methane Activation: A Computational Exploration of CNC-Ligated Iron Catalysts

Bruce M. Prince

Center for Catalysis Computational Research (3CR), Department of Chemistry, Texas Southern University, 3100 Cleburne Street, Houston, TX 77004

Abstract: This study employs DFT at the APFD/def2-TZVP level, with SMD solvation in THF, to investigate the catalytic activation of methane by $[(\kappa^3\text{-CNC})\text{Fe}(\text{N}_2\text{O})]^{2+}$ cation complexes. The catalytic mechanism encompasses three key steps: oxygen atom transfer (OAT), hydrogen atom abstraction (HAA), and oxygen radical rebound (ORR). Computational results identify OAT as the rate-determining step, with activation barriers of **-10.2 kcal/mol** and **5.0 kcal/mol** for $\kappa^1\text{-O-}$ and $\kappa^1\text{N-}$ bound intermediates in the gas and solvent phases, respectively. Methane activation proceeds via HAA, with energy barriers of **16.0–25.2 kcal/mol** depending on the spin state and solvation, followed by ORR, which occurs efficiently with barriers as low as **6.4 kcal/mol**. The triplet ($S = 1$) and quintet ($S = 2$) spin states exhibit critical roles in the catalytic pathway, with intersystem crossing facilitating optimal reactivity. Spin density analysis highlights the oxyl radical character of the $\text{Fe}^{\text{IV}}=\text{O}$ intermediate as essential for activating methane's strong C–H bond. These findings underscore the catalytic potential of CNC-ligated iron complexes for methane functionalization and demonstrate their dual environmental benefits by utilizing methane and reducing nitrous oxide, a potent greenhouse gas.

Keywords: iron-oxo; iron-oxyl; oxo-cation; methane carbon-hydrogen activation; radical; oxygen radical rebound; methanol; oxo; oxyl; hydrogen atom abstraction; HAA; hydrogen atom transfer; HAT; and intersystem crossing

INTRODUCTION

The catalytic transformation of methane, [1–5] a critical yet challenging step in chemical synthesis, holds promise for producing value-added chemicals like methanol [5–13]. Despite its abundance and potential as a versatile feedstock, methane's high carbon–hydrogen (C–H) bond dissociation enthalpy (BDE) (~105 kcal/mol) makes its functionalization energetically demanding [1–5,14–19]. This challenge has driven significant research into developing efficient catalysts capable of overcoming this barrier under mild conditions [20–24].

Simultaneously, nitrous oxide (N_2O), which is a potent greenhouse gas with a global warming potential approximately 300 times greater than carbon dioxide possesses a significant environmental challenge [25–29]. Emissions of N_2O originate from both natural sources, such as microbial soil and ocean activity, and anthropogenic activities like agricultural fertilization and industrial processes. Beyond its contribution to climate change, N_2O is a known ozone-depleting substance, emphasizing the urgent need for mitigation strategies [30–34].

Catalysts capable of utilizing N_2O as an oxidant for methane activation offer a dual benefit: [35] reducing N_2O concentrations while achieving selective methane functionalization [35]. The thermodynamic properties of N_2O make it an attractive oxygen donor, with its Gibbs free energy of dissociation ($\Delta G = -19$ kcal/mol) indicating favorable oxygen atom transfer (OAT) [36–40]. The strong $\text{N}\equiv\text{N}$ bond (bond dissociation enthalpy = 113 kcal/mol) and weaker $\text{N}-\text{O}$ bond (~39 kcal/mol) suggest that N_2O can effectively participate in catalytic cycles involving oxygen transfer [41–43].

1. Among potential catalysts, transition metal complexes supported by pyridine(dicarbene)pincer (κ^3 -CNC) ligands have emerged as promising candidates [44]. These ligands, derived from N-heterocyclic carbenes (NHCs), exhibit strong σ -donating and π -accepting properties, stabilizing high-valent metal species essential for challenging transformations [45–55]. A specific focus of this study is the simplified CNC ligand framework, which omits BR_2 appendages [50]. This design enables direct comparisons with previously studied systems, such as the BR_2 -functionalized CNC ligands explored by

Kiernicki et al. and Zimmer et al. [50,51,56] Kiernicki's work investigated CNC ligands with bulky allyl and BR_2 [50] groups to examine their steric and electronic effects on iron-mediated transformations, while Zimmer and Danopoulos analyzed similar systems in the context of small-molecule activation [50,51,57]. These prior studies provided valuable insights into ligand modifications but introduced steric hindrance and competing interactions that may obscure the primary coordination effects, for example C-H activation [13].

The simplified CNC ligand design in this study offers several advantages:

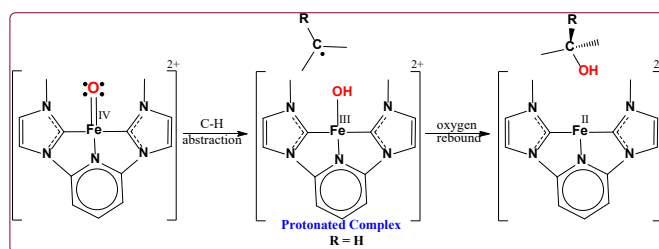
1. **Electronic Flexibility:** The CNC framework offers strong σ -donation and π -acceptance, stabilizing high-valent iron-oxo intermediates crucial for OAT and methane C-H activation. The absence of BR_2 groups eliminates potential electronic interferences, allowing the study to focus on primary metal-ligand interactions [58].
2. **Steric Profile:** Excluding bulky BR_2 substituents ensures a compact coordination environment around the iron center. This steric simplicity reduces hindrance at the active site, facilitating efficient catalytic turnover [50].
3. **Catalyst Modularity:** The simplified ligand design enables direct comparisons with previously studied systems that included BR_2 groups, isolating the effects of the primary coordination sphere. This approach provides clearer mechanistic insights into the role of the Fe center.[59]
4. **Suitability for High-Valent Oxo Complexes:** The CNC ligand's electronic properties support the stabilization of $\text{Fe}^{\text{IV}}=\text{O}$ intermediates, which are critical for methane C-H activation. Excluding BR_2 substituents avoids secondary interactions that might introduce competing pathways, simplifying mechanistic investigations [36,60–64].

These attributes make the CNC-ligated iron complexes ideal candidates for exploring methane activation and nitrous oxide utilization under mild conditions, [59] **Scheme 1**. This study employs density functional theory (DFT) to investigate the catalytic potential of $[(\kappa^3\text{-CNC})\text{Fe}(\text{N}_2\text{O})_2]^+$ complexes are summarized in **Scheme 1**. [44] The mechanism involves three key steps: OAT [36–40], hydrogen atom abstraction (HAA), [65–73] and oxygen radical rebound (ORR) [74–76] that is facilitated by high-valent $\text{Fe}^{\text{IV}}=\text{O}$ intermediates. Spin-state dynamics, including intersystem crossing (ISC) between quintet ($S = 2$) and triplet ($S = 1$) states, play a central role in determining reaction energetics.

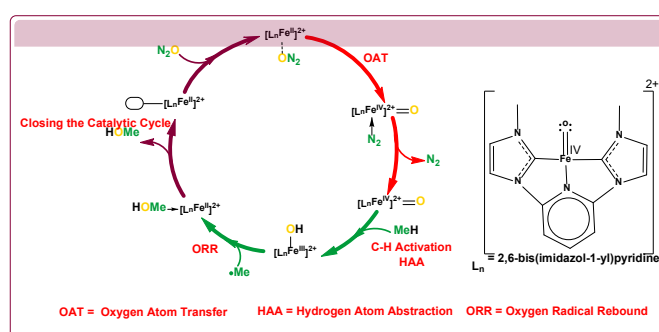
Through computational modeling, this research aims to:

1. Examine the impact of spin states on methane activation pathways.
2. Assess the activation barriers for OAT, HAA, and ORR steps.
3. Explore the role of CNC ligands in stabilizing reactive intermediates and facilitating efficient catalysis.

By addressing the dual challenges of methane activation and N_2O mitigation, this work offers insights into sustainable catalytic processes that align with environmental and industrial goals. **Scheme 2** outlines the proposed catalytic pathway for methane C-H activation, highlighting the energetic barriers for each step. The complete reaction mechanism and its spin-state-dependent energetics are depicted in **Scheme 2**.



Scheme 1. General reaction cycle for methane C–H activation via $[(\kappa^3\text{CNC})\text{Fe}(\text{N}_2\text{O})]^{2+}$ complexes, involving OAT, HAA, and ORR. The oxygen atom of N_2O is coordinated trans to the pyridine nitrogen atom of the $\kappa^3\text{-CNC}$ ligand, facilitating C–H activation.



Scheme 2. Proposed catalytic pathway for methane functionalization by $[(\kappa^3\text{CNC})\text{Fe}(\text{N}_2\text{O})]^{2+}$ complexes, including key transition states for OAT, HAA, and ORR. Energetics are calculated for singlet, triplet, and quintet spin states.

2. COMPUTATIONAL METHODS:

This study employed density functional theory (DFT) calculations to investigate the methane C–H activation [77] mechanism mediated by $[(\kappa^3\text{-CNC})\text{Fe}^{\text{II}}(\text{N}_2\text{O})]^{2+}$ cation complexes. The methodology was designed to provide a comprehensive understanding of reaction energetics, spin-state dynamics, and mechanistic pathways.

2.1. Level of Theory

The Austin-Frisch-Petersson functional with dispersion corrections (APFD) was used in combination with the def2-TZVP basis set for all geometry optimizations and single-point energy calculations. The APFD functional was selected due to its proven reliability in modeling transition metal complexes, particularly those involving high-valent iron species and non-covalent interactions [78,79].

Unlike traditional functionals such as B3LYP [80–83] or M06, [84] which often require additional empirical dispersion corrections (e.g., Grimme's D3 correction), APFD [85] natively incorporates dispersion effects, ensuring a consistent and accurate treatment of long-range interactions. Dispersion interactions play a critical role in stabilizing intermediates and transition states in the catalytic cycle, particularly during steps such as OAT, HAA, and ORR. The TSs were authenticated using intrinsic reaction coordinate (IRC) methods [86],

APFD [85] also excels in capturing subtle electronic energy differences between spin states, which is essential for this study given the importance of ISC between quintet ($S = 2$) and triplet ($S = 1$) states. These spin-state transitions heavily influence the reaction energetics and mechanistic pathways of methane activation and nitrous oxide utilization. By contrast, B3LYP [80] or M06,[84] have demonstrated limitations in accurately describing high-spin systems or the energetics of multi-reference states without significant adjustments [87,88].

Moreover, APFD [85] combines computational efficiency with accuracy, making it suitable for extensive modeling of large and complex systems like CNC-ligated iron complexes. The functional's

compatibility with the SMD [89] implicit solvation model further enhances its applicability to reactions in polar solvents such as THF ($\epsilon = 7.4257$), which plays a crucial role in stabilizing charged species and transition states.

2.2. Geometric Optimization and Frequency Analysis

All geometries, including intermediates and transition states, were optimized at the APFD/def2-TZVP/Anonymous [90] level using fine numerical integration grids and tight convergence criteria. Frequency analysis was performed to confirm the nature of each stationary point, with minima exhibiting no imaginary frequencies and transition states showing a single imaginary frequency corresponding to the reaction coordinate. Intrinsic reaction coordinate (IRC) calculations were conducted to validate the connectivity between reactants, transition states, and products [86,91].

2.3. Spin-State Considerations

To explore the role of spin multiplicity in the reaction pathways, calculations were performed for singlet ($S = 0$), triplet ($S = 1$), and quintet ($S = 2$) spin states at each step of the reaction. Mulliken population analysis was employed to analyze spin density distributions and electronic configurations, providing insights into the localization of unpaired electrons. ISC pathways were evaluated to assess their influence on reaction energetics and spin-state transitions.

2.4. Energetic Calculations

Gibbs free energies (ΔG) were computed at 298.15 K and 1 atm, incorporating thermal corrections and solvation effects. Energies are reported relative to the separated reactants ($\text{NHC-Fe} + \text{N}_2\text{O}$ and $\text{NHC-Fe=O} + \text{CH}_4$). The relative Gibbs free energy profiles were used to identify the rate-determining steps and evaluate the overall feasibility of the catalytic pathways.

2.5. Computational Model

The pyridine(dicarbene)pincer ($\kappa^3\text{-CNC}$) ligand was modeled with methyl substituents on the nitrogen atoms to reduce computational cost while preserving the ligand's electronic properties. This simplified model allowed for accurate investigation of the catalytic system, focusing on the primary coordination environment of the Fe center [50,52,92].

2.6. Reaction Pathways Investigated

The study examined three critical steps in methane activation:

1. **Oxygen Atom Transfer (OAT):** Coordination of N_2O to the Fe center and oxygen atom transfer to form the high-valent $\text{Fe}^{\text{IV}}=\text{O}$ intermediate.
2. **Hydrogen Atom Abstraction (HAA):** Interaction of the $\text{Fe}^{\text{IV}}=\text{O}$ species with methane to cleave the C–H bond.
3. **Oxygen Radical Rebound (ORR):** Rebound of the hydroxyl group with the methyl radical to yield methanol.

2.7. Software and Computational Resources

All calculations were performed using the Gaussian 16 software suite with access to high-performance computing resources [78]. Cartesian coordinates of all optimized geometries and the corresponding calculated energy values are provided in the **Supporting Information (SI)**.

3. RESULTS AND DISCUSSION

1. $[(\text{CNC})\text{Fe}^{\text{II}}]^{2+}$ Cation Complexes

The $[(\kappa^3\text{-CNC})\text{Fe}^{\text{II}}]^{2+}$ cation complex serves as the foundational structure for the catalytic cycle, with its geometric and electronic properties providing critical insights into reactivity. Optimized

geometries for the singlet ($S = 0$), triplet ($S = 1$), and quintet ($S = 2$) spin states reveal significant differences in bond lengths, bond angles, and spin density distributions, as summarized in **Figure 1** and **Table 1**.

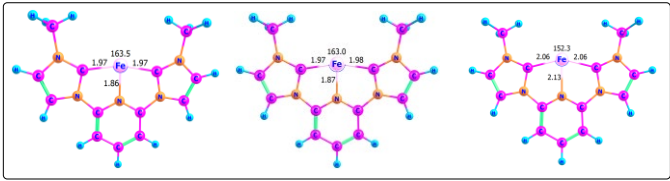


Figure 1. Optimized geometries of $[(\kappa^3\text{-CNC})\text{Fe}^{\text{II}}]^{2+}$ cation complexes in singlet ($S = 0$), triplet ($S = 1$), and quintet ($S = 2$) spin states, respectively. Bond lengths are given in Å, and bond angles in degrees. The quintet state shows longer bond lengths and wider angles, reflecting the influence of spin multiplicity on molecular geometry.

Table 1. Key geometric parameters (bond lengths in Å, bond angles in degrees) and spin density distributions (e^-) for $[(\kappa^3\text{-CNC})\text{Fe}^{\text{II}}]^{2+}$ cation complexes across singlet ($S = 0$), triplet ($S = 1$), and quintet ($S = 2$) spin states.				
Spin State	Fe–C (Å)	Fe–N (Å)	C–Fe–C (°)	Spin Density (Fe, e^-)
Singlet ($S = 0$)	1.97	1.86	163.5	0.00
Triplet ($S = 1$)	1.97	1.87	163.0	2.17
Quintet ($S = 2$)	2.06	2.13	152.3	4.00

1.1. Geometric and Spin-State Analysis

The geometric parameters of the $[(\kappa^3\text{-CNC})\text{Fe}]^{2+}$ complex reveal significant variations across the quintet ($S = 2$), triplet ($S = 1$), and singlet ($S = 0$) spin states, reflecting differences in metal-ligand interactions. In the quintet state, the Fe–C and Fe–N bonds are notably elongated, indicating weaker coordination due to the increased spin density localized on the Fe center. Specifically, the Fe–C bond length increases from 1.97 Å in the singlet state to 2.06 Å in the quintet state, while the Fe–N bond length expands from 1.86 Å to 2.13 Å. Additionally, the C–Fe–C bond angle is widest in the quintet state (152.3°), likely due to steric effects from the distributed spin density.

In respect, the triplet state exhibits shorter bond lengths (Fe–C = 1.97 Å, Fe–N = 1.87 Å) and a narrower bond angle (163.0°), reflecting stronger metal-ligand interactions. The singlet state is the most compact, with Fe–C and Fe–N bond lengths closely matching those of the triplet state (Fe–C = 1.97 Å, Fe–N = 1.86 Å) and a slightly narrower bond angle of 163.5°. These observations align well with previous computations for smaller Fe^{2+} complexes [93].

1.1. Electronic Structure and Reactivity Implications

Spin density analysis highlights significant differences in the electronic structure across spin states. In the quintet state, the Fe center exhibits high spin density (4.00 e^-), consistent with its $d[6]$ high-spin electronic configuration.[94] This configuration results in weaker bonding interactions and elongated bonds. The triplet state, with a spin density of 2.17 e^- , demonstrates more delocalized electronic interactions, leading to stronger bonding and a more stable geometry. The singlet state,

with no unpaired electrons, represents a fully closed-shell configuration, exhibiting the most compact geometry. The geometric and electronic differences between these spin states are critical for the catalytic cycle. The quintet state, with its higher spin density and weaker bonding, facilitates the initial coordination of N₂O and [36–40]. Conversely, the triplet state, with its lower energy and more stable interactions, is better suited for subsequent steps in the catalytic pathway, such as methane C–H activation.

1.1. Conclusion for [(CNC)Fe^{II}]²⁺ Cation Complexes

The structural and electronic analysis of [(κ^3 -CNC)Fe^{II}]²⁺ complexes highlights the interplay between spin states and molecular geometry. The high-spin quintet state provides a reactive intermediate for the initial stages of the catalytic cycle, while the triplet state stabilizes intermediates in subsequent steps. These findings underscore the importance of spin-state control in enabling efficient methane activation [95,96].

2. Coordination and Energetics of N₂O to [(κ^3 -CNC)Fe^{II}]²⁺ Cation Complex

The coordination of nitrous oxide (N₂O) to the [(κ^3 -CNC)Fe^{II}]²⁺ cation complex is a pivotal step in the catalytic cycle, forming the precursor necessary for oxygen atom transfer (OAT). Computational results reveal that the energetic preference between the κ^1 -N-bound and κ^1 -O-bound configurations depends on both the phase and the spin state of the system.

In the gas phase, the quintet (*S* = 2) spin state serves as the ground state, favoring the κ^1 -O-bound configuration with a Gibbs free energy of **–10.2 kcal/mol**, compared to **2.0 kcal/mol** for the κ^1 -N-bound relative to κ^1 -O-bound. Conversely, in tetrahydrofuran (THF), solvation effects stabilize the κ^1 -N-bound intermediate, with a relative Gibbs free energy of **5.0 kcal/mol**, compared to **3.7 kcal/mol** for the κ^1 -O-bound relative to κ^1 -N-bound. This solvent-driven stabilization of the κ^1 -N-bound intermediate highlights the critical role of solvation effects in modulating the coordination environment and influencing spin-state energetics.

The κ^1 -N-bound intermediate is characterized by a Fe–N bond length of **2.28 Å**, a slightly shortened N–O bond length of **1.15 Å**, and a nearly linear Fe–N–N bond angle of **167.9°**, effectively positioning the oxygen atom for transfer to the Fe center. In contrast, the κ^1 -O-bound configuration features a Fe–O bond length of **1.91 Å** and a N–O bond length of **1.13 Å**, with a Fe–O–N angle of **143.7°**, reflecting the distinct bonding modes between the configurations.

Despite the mild endergonic nature of N₂O coordination in the solvent phase (ΔG = **5.0 kcal/mol**), the κ^1 -N-bound intermediate plays a critical role as the precursor to the high-valent Fe^{IV}=O species formed during OAT. These results underscore the importance of evaluating both gas-phase and solvent-phase energetics to fully understand catalytic intermediates. Further details of the κ^1 -O-bound configuration are provided in the **Supporting Information (SI)**.

2.1. Geometric Features of the Quintet State

The optimized geometry of the κ^1 -N-bound quintet (*S* = 2) state is depicted in **Figure 2**. In this configuration, nitrous oxide (N₂O) coordinates through its nitrogen atom to the Fe center, resulting in a **Fe–N bond length of 2.28 Å** and a **slightly shortened N–O bond length of 1.15 Å**. This shortening suggests that the oxygen atom is pulling electron density away from the nitrogen atom, increasing the δ^- character of the oxygen and strengthening the N–O bond. The nearly linear **Fe–N–N bond angle of 167.9°** effectively positions the oxygen atom for transfer to the Fe center during the subsequent oxygen atom transfer (OAT) step [71,97]. The spin density in this configuration is primarily localized on the Fe center (**3.94 e⁻**), consistent with its high-spin d[6] electronic configuration [94]. This spin localization enhances the Fe–N₂O interaction, allowing for electron donation from the metal center to the N₂O antibonding, which could facilitate subsequent bond cleavage and reorganization during OAT. This geometric and electronic arrangement highlights the critical role of the high-spin quintet state in activating N₂O and positioning the system for efficient catalytic turnover.

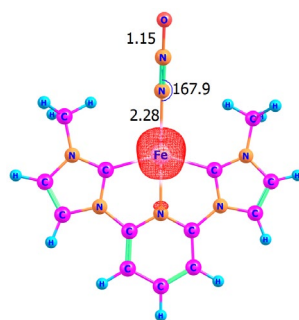
[5][NHC-Fe-N₂O]

Figure 2. Optimized ground state geometry of the κ^1 -N-bound $[(\kappa^3\text{-CNC})\text{Fe}^{\text{II}}(\text{N}_2\text{O})]^{2+}$ cation complex in the quintet ($S = 2$) spin state. Bond lengths are given in Å, and bond angles in degrees. The near-linear Fe–N–N bond angle (167.8°) aligns the oxygen atom for OAT. The high-spin density values (e^-) are shown on the Fe center to ($\sim 3.94 e^-$). The contour value of the spin density plot is 0.020.

2.1. Conclusion for N₂O Coordination

The coordination of N₂O to $[(\kappa^3\text{-CNC})\text{Fe}^{\text{II}}]^{2+}$ highlights the significance of spin-state effects and molecular geometry in the catalytic process. The exergonic nature of this step in the gas phase, combined with the near-linear Fe–N–N configuration, positions the κ^1 -N-bound intermediate as a key precursor for subsequent OAT. Despite mild energetic in the solvent phase, the electronic and structural properties of this intermediate underscore its pivotal role in the catalytic pathway.

3. Oxygen Atom Transfer of N₂O to Form Oxo Fe^{IV} Cation

OAT from nitrous oxide (N₂O) to the $[(\kappa^3\text{-CNC})\text{Fe}^{\text{II}}]^{2+}$ complex is a critical step in the catalytic cycle, leading to the formation of the high-valent Fe^{IV}=O oxo species. This step involves significant bond reorganization at the transition state (TS) and is identified as the rate-determining step due to its high energy barrier.

3.1. Geometry and Transition State of OAT

The optimized geometry of the OAT transition state in the **triplet ($S = 1$)** spin state reveals key structural features:

- **Fe–O Bond Length:** 1.83 Å, reflecting partial formation of the Fe–O bond.
- **O–N Bond Length:** 1.40 Å, showing significant elongation as the N–O bond undergoes cleavage.
- **N–N Bond Length:** 1.14 Å, consistent with the release of N₂.
- **Fe–O–N–N Bond Angle:** 180.0° , indicative of a linear arrangement facilitating efficient oxygen transfer and nitrogen release.

3.2. Spin-State Dependence of OAT

The resulting Fe^{IV}=O intermediate features a strong Fe=O double bond (1.62 Å), **Figure 4**, with pronounced oxo character and partial radical spin density ($0.87 e^-$ on the oxygen atom). This intermediate is pivotal for enabling methane C–H activation in subsequent catalytic steps. The OAT step exhibits a pronounced spin-state dependence, significantly influencing the energetics of the catalytic pathway. Computational results reveal that in the gas phase, the triplet ($S = 1$) spin state is energetically favored, with a Gibbs free energy barrier of $\Delta G^\ddagger = 26.3 \text{ kcal/mol}$, compared to $\Delta G^\ddagger = 36.9 \text{ kcal/mol}$ for the quintet ($S = 2$) spin state, as shown in **Scheme 3**. This lower barrier highlights the triplet pathway as the preferred route for initiating the catalytic cycle under gas-phase conditions.

The reduced barrier for the triplet state arises from its ability to better stabilize the transition state geometry through enhanced electronic reorganization during bond-breaking and bond-forming processes. In contrast, the higher barrier for the quintet state can be attributed to the increased spin

density localized on the Fe center, which raises the energetic cost of rearranging bonding interactions during OAT.

These findings underscore the critical role of spin-state dynamics in determining reaction energetics. By favoring the triplet state for the initial activation step, the catalytic system achieves a more accessible pathway for the OAT process, setting the stage for subsequent methane functionalization.

3.3. Solvent Effects and Alternative Solvent Recommendations

In the THF solvent phase, the Gibbs free energy barrier for the OAT step increases significantly, rising to $\Delta G^\ddagger = 53.2 \text{ kcal/mol}$, as shown in **Scheme 4**. This substantial increase indicates that solvation effects destabilize the Fe complex during this step. The destabilization likely stems from THF's solvation of the reactants, which preferentially lowers the energy of the initial state relative to the transition state, resulting in higher overall free energy barriers.

While THF is commonly employed due to its moderate polarity and compatibility with transition metal complexes, its impact on the energetics of critical steps such as OAT and HAA suggests the need to explore alternative solvents. Optimizing the solvation environment could mitigate these destabilizing effects and enhance catalytic efficiency.

3.4. Alternative Solvents:

To address the limitations observed with THF, several alternative solvents are proposed:

1. Polar Aprotic Solvents:

- **Acetonitrile (CH₃CN)**: A highly polar, non-coordinating solvent that minimizes interactions with the Fe center while providing strong stabilization of polar intermediates and transition states.
- **Dimethylformamide (DMF)**: Offers high polarity and strong stabilization for charged species but may introduce undesired interactions in some catalytic systems.

2. Dimethyl Sulfoxide (DMSO):

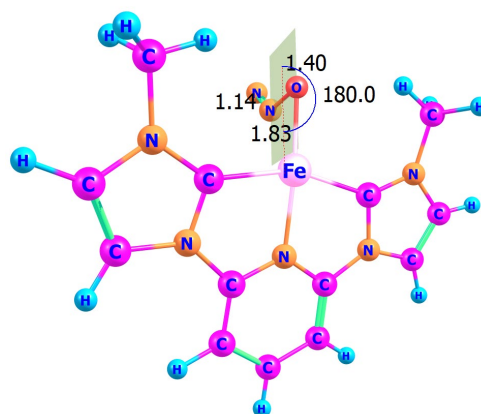
- DMSO effectively stabilizes charged intermediates due to its high polarity. However, its coordinating nature may lead to unintended interactions with the Fe center, requiring careful evaluation for compatibility with this system.

3. Moderate Polarity Solvents:

- **Dichloromethane (DCM)** and **ethyl acetate (EtOAc)** strike a balance between polarity and inertness. Their moderate polarity can stabilize intermediates without significant coordination to the Fe center, making them attractive alternatives.

4. Nonpolar Solvents:

- **Toluene** and other nonpolar solvents may reduce solvation effects and potentially lower transition state energies. Combining these with polar co-solvents could fine-tune the solvation environment to achieve optimal catalytic performance.



[3][OAT-TS1]‡

Figure 3. Optimized geometry of the oxygen atom transfer (OAT) transition state in the triplet ($S = 1$) spin state. Bond lengths are given in Å. The near-linear Fe–O–N–N bond alignment facilitates efficient oxygen atom transfer and N_2 release.

3.5. Conclusion of OAT Mechanism

The choice of solvent significantly influences the energetics of the reaction cycle, particularly for steps like OAT. Polar aprotic solvents such as acetonitrile and moderately polar solvents like DCM offer promising alternatives for mitigating the destabilizing effects observed in THF. Nonpolar environments, potentially augmented with polar co-solvents, also present viable options. Selecting the optimal solvent is critical for minimizing free energy barriers and maximizing the overall catalytic efficiency.

4. Structure and Properties of the $Fe^{IV}=O$ Complex

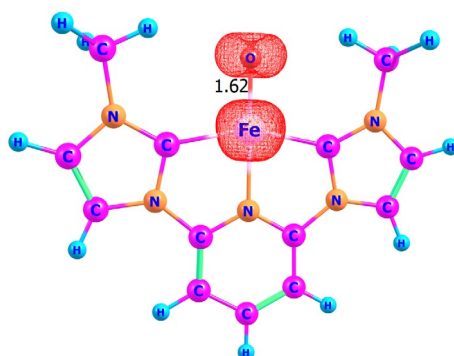
The $Fe^{IV}=O$ oxo complex, formed during the OAT step, serves as a key reactive intermediate in the catalytic cycle. This species exhibits distinct geometric and electronic properties that are crucial for facilitating subsequent methane C–H activation via hydrogen atom abstraction (HAA).

4.1. Geometric Features

The optimized geometry of the $Fe^{IV}=O$ complex reveals key structural characteristics, as summarized below:

- **Fe=O Bond Length:** 1.62 Å, indicative of a strong double bond with significant oxo character.
- **CNC Ligand Coordination:** The CNC ligand maintains a distorted square planar geometry around the Fe center, with the oxo ligand occupying an axial position.
- **Spin-State Configurations:** Geometric variations between the triplet ($S = 1$) and quintet ($S = 2$) states highlight the influence of spin state on bond lengths and coordination environment.

5. Oxo/Oxyl Characterization



[5][OXO/OXYL]

Figure 4. Optimized ground state geometry and spin density distribution of the $\text{Fe}^{\text{IV}}=\text{O}$ complex in the quintet ($S = 2$) spin state. Bond lengths are given in Å, and spin density values (e^-) are shown on the Fe center and O atom. The oxyl radical character of the oxygen atom ($\sim 0.87 e^-$) and the high-spin Fe center ($\sim 3.16 e^-$) make this complex a highly reactive intermediate for methane activation. The contour value of the spin density plot is 0.020.

5.1. Spin-State Energetics

The $\text{Fe}^{\text{IV}}=\text{O}$ complex demonstrates spin-state-dependent stability:

1. **Quintet ($S = 2$) State:** The quintet spin state is the ground-state configuration for the $\text{Fe}^{\text{IV}}=\text{O}$ species. The high spin density ($3.16 e^-$ on Fe and $0.87 e^-$ on O) reflects the distribution of unpaired electrons, which enhances the oxyl radical character of the oxygen atom. This configuration is stabilized by the strong σ -donation from the oxo group and π -backbonding interactions with the CNC ligand.
2. **Triplet ($S = 1$) State:** While the triplet state plays a critical role during the OAT step, it lies higher in energy (by $\sim 3\text{--}7$ kcal/mol depending on the environment phase) compared to the quintet state for the $\text{Fe}^{\text{IV}}=\text{O}$ species. This energy gap facilitates a spin flip to the quintet state after OAT, enabling the complex to adopt its thermodynamically preferred configuration.

5.2. Electronic Structure

The electronic structure of the $\text{Fe}^{\text{IV}}=\text{O}$ complex is characterized by significant oxo radical character, as evidenced by the spin density distribution:

- **Iron Center (Fe):** Spin density of $3.17 e^-$ in the quintet state, consistent with its $d[4]$ configuration.
- **Oxo Ligand (O):** Partial spin density of $0.87 e^-$, indicative of an oxyl radical. This feature is critical for activating methane via HAA.

The strong $\text{Fe}=\text{O}$ bond and oxyl radical nature enhance the reactivity of the complex, making it a potent oxidant capable of cleaving the strong C–H bond in methane.

5.3. Reactivity Implications

The $\text{Fe}^{\text{IV}}=\text{O}$ oxo species is uniquely suited for methane activation due to its electronic and spin properties:

1. **Oxo Radical Rebound:** The oxyl radical character facilitates rapid rebound with the methyl radical during the oxygen radical rebound (ORR) step, ensuring efficient formation of methanol.
2. **Hydrogen Atom Abstraction (HAA):** The $\text{Fe}^{\text{IV}}=\text{O}$ species initiates HAA by abstracting a hydrogen atom from methane, driven by its strong oxidizing potential and spin-state reactivity.

5.4. Conclusion Oxo/Oxyl Characterization

The $\text{Fe}^{\text{IV}}=\text{O}$ oxo complex is a critical intermediate in the catalytic cycle, with its structure and spin-state properties directly influencing its reactivity. The ground-state quintet configuration, stabilized by strong $\text{Fe}=\text{O}$ bonding and oxo radical character, sets the stage for efficient methane C–H activation. The spin flip from the triplet state after OAT further underscores the dynamic role of spin-state transitions in enabling the catalytic mechanism.

6. Methane C–H Activation by Oxo/Oxyl Cation Complex

Methane C–H activation by the $\text{Fe}^{\text{IV}}=\text{O}$ oxo cation complex involves two pivotal steps: **HAA** and **ORR**, culminating in the formation of methanol. The catalytic efficiency stems from the electronic and geometric properties of the $\text{Fe}^{\text{IV}}=\text{O}$ intermediate, with spin-state dynamics playing a significant role. **Figures 5 and 6** illustrate the transition state (TS) geometries for HAA and ORR, while **Table 2** and **Schemes 3 and 4** summarize the energetics and free energy profiles.

6.1. Hydrogen Atom Abstraction (HAA)

The HAA step is initiated when the oxygen atom of the $\text{Fe}^{\text{IV}}=\text{O}$ complex abstracts a hydrogen atom from methane. This process involves the formation of an O–H bond and the elongation of the C–H bond.

6.2. Geometric Features:

The transition state (TS) geometries for HAA by the $\text{Fe}^{\text{IV}}=\text{O}$ complex reveal distinct structural features for the quintet ($S = 2$) and triplet ($S = 1$) spin states, highlighting their different reactivity profiles. In the quintet state, the Fe–O bond length is slightly elongated at 1.72 Å, reflecting a partially formed O–H bond (1.22 Å) and a C–H bond stretched to 1.33 Å. The Fe–O–H bond angle of 94.1° indicates a compact geometry that facilitates interaction between the $\text{Fe}^{\text{IV}}=\text{O}$ center and the incoming hydrogen atom. In contrast, the triplet state exhibits a shorter Fe–O bond length of 1.67 Å, with a more extended O–H bond of 1.37 Å and a slightly compressed C–H bond of 1.20 Å. The Fe–O–H bond angle in the triplet state is 114.0°, suggesting a more open transition state geometry that may enhance the accessibility of the substrate. These differences underscore the spin-dependent nature of the HAA step, with the triplet state favoring tighter bonding at the oxygen center and the quintet state enabling a more compact and symmetric transition state geometry.

6.3. Spin Densities:

The spin density distribution provides critical insights into the electronic structure of the $\text{Fe}^{\text{IV}}=\text{O}$ complex and its reactivity during hydrogen atom abstraction (HAA). In the quintet state ($S = 2$), the Fe center retains a spin density of 2.91 e^- , while the oxygen atom exhibits a spin density of 0.67 e^- . This distribution reflects the partial transfer of electron density during HAA, with the oxygen atom displaying moderate oxyl radical character. In contrast, the triplet state ($S = 1$) shows a slightly lower Fe spin density of 2.87 e^- , accompanied by a reduced oxygen spin density of 0.32 e^- . This stronger oxyl radical character in the triplet state highlights its enhanced ability to facilitate bond-breaking and bond-forming processes, making it more reactive compared to the quintet state. The differences in spin density distributions underscore the critical role of spin-state dynamics in determining the reactivity and efficiency of the catalytic cycle. The higher oxyl radical character in the triplet state aligns with its lower energy barrier for HAA, further emphasizing the triplet state as the preferred pathway for methane activation.

6.4. Energetics:

In the gas phase, the triplet state exhibits a lower free energy barrier than the quintet state, with barriers of 16.0 and 18.0 kcal/mol, respectively. In THF, the barriers increase to 23.5 and 25.2 kcal/mol

for the triplet and quintet states, respectively. This data indicates that HAA is energetically more favorable in the gas phase than in the solvent phase, regardless of the spin state.

A notable trend observed is the significantly higher transition state (TS) energies in THF compared to the gas phase. This difference arises from the differential stabilization provided by the solvent. As a polar medium, THF stabilizes the reactants, particularly the $\text{Fe}^{\text{IV}}=\text{O}$ complex, through favorable solvation interactions with its polarized nature. However, the transition states, characterized by strained geometries and substantial charge redistribution, do not benefit equally from these solvation effects. Consequently, the relative Gibbs free energy barriers for both HAA and ORR increase in the solvated phase. This trend underscores the nuanced role of the solvent environment in modulating the energetics and mechanisms of catalytic pathways, emphasizing the importance of solvent selection in optimizing reaction conditions.

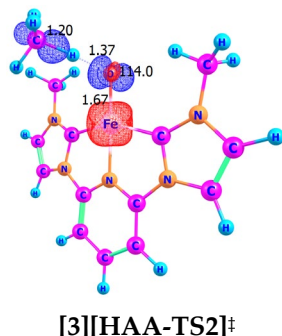
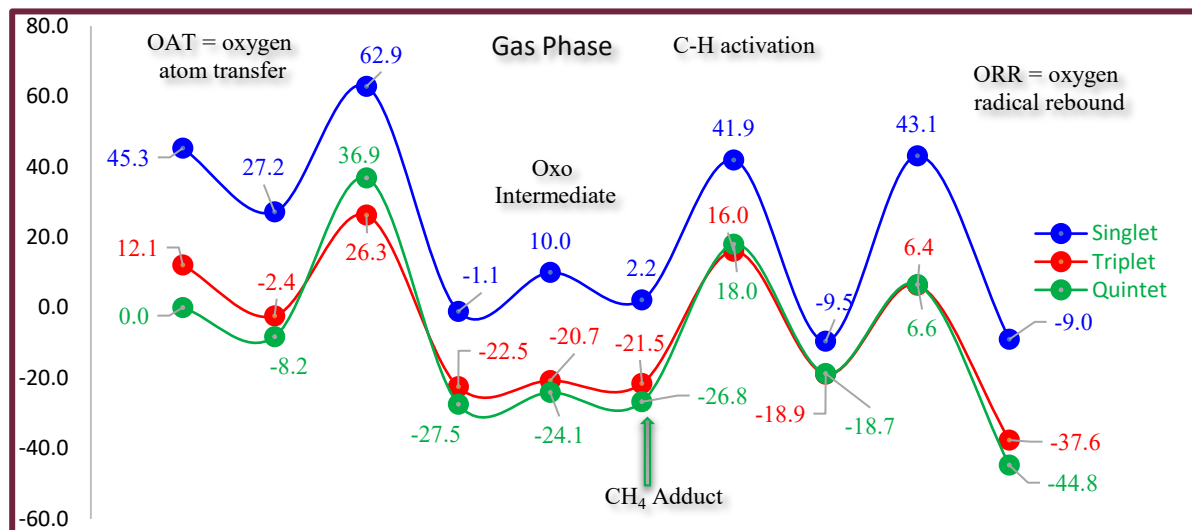
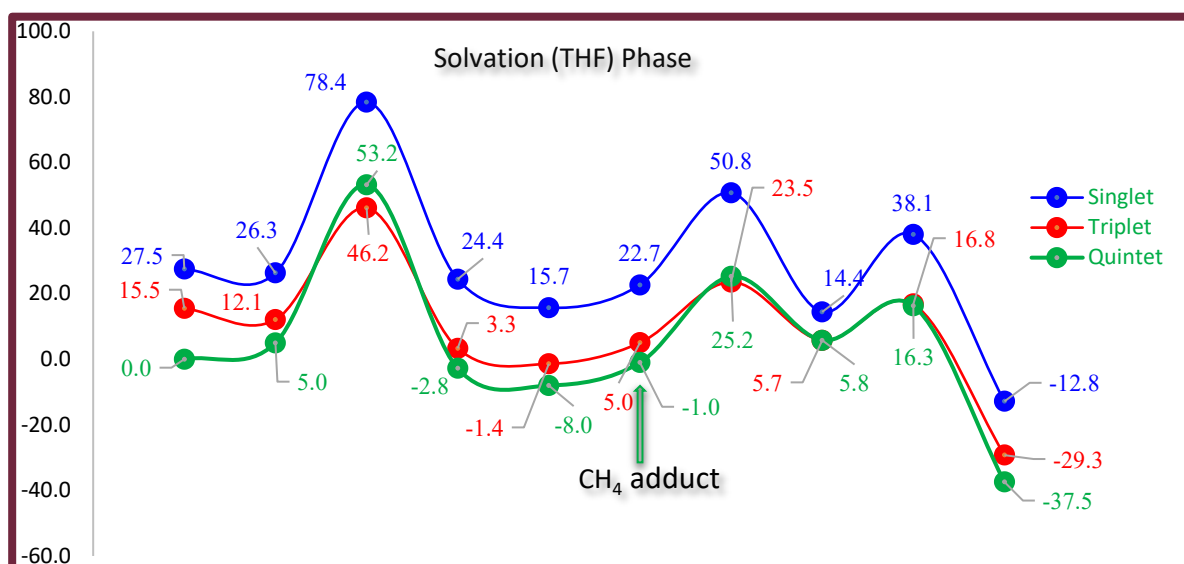


Figure 5. Optimized transition state geometry for HAA by the $\text{Fe}^{\text{IV}}=\text{O}$ oxo complex in the triplet ($S = 1$) spin states. Bond lengths are given in Å, and bond angles in degrees. Red = positive spin density and Blue = negative spin density. The contour value of the spin density plot is 0.020.



Scheme 3. Free energy profile for the catalytic cycle of methane activation by the $\text{Fe}^{\text{IV}}=\text{O}$ complex in the gas phase. The energy barriers for the OAT, HAA, and ORR steps are shown for the singlet (blue), triplet (red), and quintet (green) spin states. Energies are reported as Gibbs free energies (ΔG) in kcal/mol, with the triplet and quintet spin states exhibiting competitive pathways, while the singlet state remains energetically less favorable. Key transition states and intermediates are highlighted along with the reaction coordinate.



Scheme 4. Free energy profile for the catalytic cycle of methane activation by the $\text{Fe}^{\text{IV}}=\text{O}$ complex in the solvation (THF) phase. The energy barriers for the OAT, HAA, and ORR steps are shown for the singlet (**blue**), triplet (**red**), and quintet (**green**) spin states. Energies are reported as Gibbs free energies (ΔG) in kcal/mol, with the triplet and quintet spin states exhibiting competitive pathways, while the singlet state remains energetically less favorable. Key transition states and intermediates are highlighted along with the reaction coordinate.

7. Oxygen Radical Rebound (ORR)

Following HAA, the methyl radical recombines with the hydroxyl group of the $\text{Fe}^{\text{III}}-\text{OH}$ intermediate, completing the catalytic cycle by forming methanol.

7.1. Geometric Features:

The transition state (TS) geometries for ORR reveal distinct features for the quintet ($S = 2$) and triplet ($S = 1$) spin states, reflecting their differing mechanistic pathways. In the quintet state, the Fe–O bond length is 1.82 Å, indicating the partial dissociation of the Fe–O bond as the O–C bond forms with a length of 2.17 Å. The Fe–O–C bond angle of 71.4° suggests a compact arrangement, facilitating efficient recombination of the hydroxyl group with the methyl radical to form methanol. Conversely, the triplet state also exhibits an Fe–O bond length of 1.82 Å but a slightly shorter O–C bond of 2.08 Å, indicative of a more flexible transition state. The Fe–O–C bond angle in the triplet state is 72.4°, reflecting a slightly more open geometry that may enhance orbital alignment for the rebound step. These structural differences underscore the spin-state dependence of the ORR mechanism, with the quintet state favoring a compact transition state geometry, while the triplet state exhibits enhanced flexibility.

7.2. Spin Densities:

In the quintet state, the Fe center exhibits a spin density of 4.01 e^- , while the oxygen atom displays negligible spin density, indicating electron pairing as the O–C bond forms during methanol generation. In the triplet state, the Fe center's spin density decreases to 0.14 e^- , and the oxygen-atom's spin density -0.50 e^- , further confirming its role as a reactant in the rebound step and its contribution to stabilizing the methanol product.

7.3. Energetics:

The ORR step, where the methyl radical recombines with the hydroxyl group of the $\text{Fe}^{\text{III}}-\text{OH}$ intermediate to form methanol, is characterized by moderate Gibbs free energy barriers. In the gas phase, the free energy barrier (ΔG^\ddagger) for the triplet ($S = 1$) state is 6.4 kcal/mol, while the quintet ($S = 2$)

state exhibits a slightly higher barrier of 6.6 kcal/mol. These values indicate that both spin states are energetically favorable for this step under gas-phase conditions. In the THF solvent phase, the free energy barriers increase significantly due to solvation effects. The triplet state shows a barrier of 16.8 kcal/mol, while the quintet state has a barrier of 16.3 kcal/mol. The smaller energy difference between the two spin states in the solvent phase suggests a reduced spin-state dependence during ORR when solvation is considered. These barriers remain accessible under typical catalytic conditions, emphasizing the feasibility of methanol formation via the ORR mechanism.

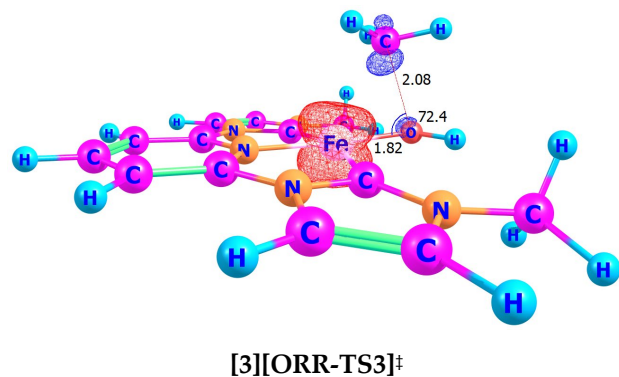


Figure 6. Optimized transition state geometries for ORR by the Fe^{III}-OH intermediate in the triplet (S = 1) spin states. Bond lengths are given in Å, and bond angles in degrees. Red = positive spin density and Blue = negative spin density. The contour value of the spin density plot is 0.020.

Table 2. Geometric and energetic parameters for HAA and ORR by the Fe^{IV}=O complex in methane activation.

Parameter	Gas Phase (Triplet)	Gas Phase (Quintet)	THF Solvent (Triplet)	THF Solvent (Quintet)
ΔG [‡] HAA (kcal/mol)	16.0	18.0	23.5	25.2
ΔG [‡] ORR (kcal/mol)	6.4	6.6	16.8	16.3
Fe–O (HAA, Å)	1.67	1.72	1.67	1.72
O–H (HAA, Å)	1.37	1.22	1.37	1.22
C–H (HAA, Å)	1.20	1.33	1.20	1.33
Fe–O–H (HAA, °)	114.0	94.1	114.0	94.1
Fe–O (ORR, Å)	1.82	1.82	1.80	1.82
O–C (ORR, Å)	2.08	2.17	2.08	2.17
Fe–O–C (ORR, °)	74.2	71.4	74.2	71.4

7.4. Conclusion

Methane activation by the $\text{Fe}^{\text{IV}}=\text{O}$ oxo complex involves efficient HAA and ORR steps. The triplet ($S = 1$) state generally provides lower barriers for HAA, while ORR exhibits reduced spin-state dependence. These results underscore the catalytic potential of CNC-ligated iron complexes for selective methane functionalization.

8. Summary

This study employs density functional theory (DFT) to investigate the catalytic activation of methane by CNC-ligated iron complexes, utilizing nitrous oxide (N_2O) as an oxidant. The computational analysis explains the detailed mechanistic steps of oxygen atom transfer (OAT), methane C–H bond activation, and methanol formation, with a particular focus on spin-state dynamics and solvation effects.

The results demonstrate that the simplified CNC ligand framework, devoid of bulky BR_2 Lewis acid appendages, effectively stabilizes high-valent Fe intermediates while maintaining catalytic efficiency. The interplay between the triplet ($S = 1$) and quintet ($S = 2$) spin states is critical in facilitating favorable reaction pathways, with intersystem crossing (ISC) providing additional versatility to the catalytic mechanism. Furthermore, solvent effects significantly impact the reaction energetics, underscoring the importance of optimizing the solvation environment to achieve enhanced catalytic performance.

These findings advance the understanding of methane functionalization, offering a dual advantage of reducing the potent greenhouse gas N_2O while enabling the selective conversion of methane into valuable chemical products. This work highlights CNC-ligated iron catalysts as a promising platform for achieving sustainable chemical transformations with environmental and industrial relevance.

9. Conclusions

This study provides a comprehensive computational investigation into the catalytic activation of methane by CNC-ligated iron complexes, leveraging nitrous oxide (N_2O) as an oxidant. Through DFT calculations, the detailed mechanistic pathways of OAT, HAA, and ORR were elucidated, highlighting the critical influence of spin-state dynamics and solvent effects.

The results reveal that the simplified CNC ligand framework effectively stabilizes high-valent Fe intermediates while maintaining catalytic efficiency. The interplay between the triplet ($S = 1$) and quintet ($S = 2$) spin states facilitates favorable reaction pathways, with intersystem crossing (ISC) enhancing the system's versatility. Solvent effects were shown to significantly influence energetics, emphasizing the importance of tailoring reaction environments for optimized catalytic performance.

These findings advance the understanding of methane functionalization, offering dual benefits: reducing the potent greenhouse gas N_2O and converting methane into value-added products like methanol. This study establishes CNC-ligated iron catalysts as a promising platform for achieving sustainable and efficient chemical transformations.

10. Prospectus

The findings of this study open several avenues for future research and practical development:

1. **Experimental Validation:** The computationally derived mechanisms and spin-state energetics provide a foundation for experimental efforts to synthesize and characterize CNC-ligated iron complexes under conditions analogous to those modeled computationally.
2. **Ligand Optimization:** Future work could explore alternative CNC ligand scaffolds or substitutions to enhance stability, selectivity, and catalytic turnover, especially for systems involving polar or nonpolar solvent environments.

3. **Solvent Engineering:** The demonstrated impact of solvation on OAT and methane activation highlights the need for further exploration of mixed solvent systems or highly nonpolar environments to optimize solvation-induced energy barriers.
4. **Broader Substrate Scope:** Beyond methane, this catalytic approach could be extended to other hydrocarbons or small molecules, broadening its applicability in chemical synthesis.
5. **Industrial Scale-Up:** Developing scalable processes for methanol production using N₂O as an oxidant could reduce reliance on conventional, energy-intensive methods like steam methane reforming, aligning with global sustainability goals.

These prospects underscore the transformative potential of CNC-ligated iron catalysts in advancing methane utilization and greenhouse gas mitigation.

In summary, this work highlights CNC-ligated iron catalysts as a compelling solution to critical environmental and industrial challenges, paving the way for more sustainable and efficient chemical transformations.

Supporting Information: Cartesian coordinates of all calculated species along with their spin multiplicities and full citation for ref 26. This material is available free of charge via the Internet at <http://pubs.acs.org>.

Acknowledgement: This work was supported in part by Texas Southern University (TSU) High Performance Computing Center (<http://hpcc.tsu.edu/>; Grant PHY-1126251). Texas Southern University Department of Chemistry, The Center for Computational Catalysis Research (3CR).

Notes: The authors declare no competing financial interest.

References

1. Zhou; Xu; Zhou; Gong; Yin; Zheng; Guo *ChemSusChem* **2011**, 4, 1095.
2. Zimmermann; Soorholtz; Bilke; Schüth *J. Am. Chem. Soc.* **2016**, 138, 12395.
3. Zerella; Mukhopadhyay; Bell *Chem. Commun.* **2004**, 1948.
4. Zerella; Kahros; Bell *J. Catal.* **2006**, 237, 111.
5. Yang; Hu; Qin *Chem. Phys.* **2006**, 330, 343–348.
6. Yamanaka; Soma; Oisuka *J. Chem. Soc., Chem. Commun.* **1995**, 2235.
7. Yuan; Wang; Wang *Ind Eng Chem Res* **2011**, 50, 6513.
8. Prince; A computational DFT study of methane CH and ammine NH activations by group 9 N-pyrrolyl complexes. **2019**, 1162, 112503.
9. Prince; Gunnoe; Cundari *Dalton Trans.* **2014**, 43, 7608–7614.
10. Prince; Cundari; Tymczak *J Phys Chem A* **2014**, 118, 11056–11061.
11. Prince; Cundari C–H Bond Activation of Methane by PtII–N-Heterocyclic Carbene Complexes. The Importance of Having the Ligands in the Right Place at the Right Time. **2012**, 31, 1042–1048.
12. Prince; Cundari *J Phys Chem A* **2013**, 117, 9245–9251.
13. Sakaki; Biswas; Sugimoto *Journal of the Chemical Society. Dalton transactions* **1997**, 803–810.
14. bond dissociation energy. [https://texsu.blackboard.com/bbcswebdav/pid-1517365-dt-content-rid-14175237_1/courses/CHEM_411-01_201910/CHEM_411-01_201910_ImportedContent_20180828124157/bond dissociation energy.pdf](https://texsu.blackboard.com/bbcswebdav/pid-1517365-dt-content-rid-14175237_1/courses/CHEM_411-01_201910/CHEM_411-01_201910_ImportedContent_20180828124157/bond%20dissociation%20energy.pdf) (accessed 10/15, 2018).
15. Jursic; Timberlake; Engel *Tetrahedron Lett.* **1996**, 37, 6473–6474.
16. Blanksby; Ellison *Acc. Chem. Res.* **2003**, 36, 255–263.
17. Gunsalus; Koppaka; Park; Bischof; Hashiguchi; Periana *Chem. Rev.* **2017**, 117, 8521–8573.
18. Sobalík; Tabor; Nováková; Sathu; Závěta *Journal of Catalysis* **2012**, 289, 164–170.

19. Prince A computational DFT study of methane CH and ammine NH activations by group 9 N-pyrrolyl complexes. **2019**, 1162, 112503.
20. Meng; Cui; Rajan; Yu; Deng; Bao *Chem* **2019**, 5, 2296–2325.
21. Prince; Cundari C–H Bond Activation of Methane by PtII–N-Heterocyclic Carbene Complexes. The Importance of Having the Ligands in the Right Place at the Right Time. **2012**, 31, 1042–1048.
22. Yuan; Wang; Wang *Ind Eng Chem Res* **2011**, 50, 6513.
23. Prince A computational DFT study of methane CH and ammine NH activations by group 9 N-pyrrolyl complexes. **2019**, 1162, 112503.
24. Paul; Musgrave *Organometallics* **2007**, 26, 793–809.
25. Fifth Assessment Report — IPCC. <https://www.ipcc.ch/assessment-report/ar5/> (accessed Jul 31, 2024).
26. Special Report on the Ocean and Cryosphere in a Changing Climate — . <https://www.ipcc.ch/srocc/> (accessed Jul 31, 2024).
27. Sixth Assessment Report — IPCC. <https://www.ipcc.ch/assessment-report/ar6/> (accessed Jul 31, 2024).
28. Bahrami; Pourfayaz; Kasaeian *Energy Reports* **2022**, 8, 2976–2988.
29. Danny Harvey *Energy Policy* **1993**, 21, 24–34.
30. Sanz-Cobena; Sánchez-Martín; García-Torres; Vallejo *Agric. , Ecosyst. Environ.* **2012**, 149, 64–73.
31. Wang; Xiong; Yan *Atmos. Environ.* **2011**, 45, 6923–6929.
32. *The effects of different mineral nitrogen fertilizer forms on N₂O emissions from arable soils under aerobic conditions*; Cuvillier Verlag: Göttingen, 2017; .
33. Jian-She; Fu-Ping; Jin-Hua; Jin-Ping; Ming-Li; Li; Cao *Agric. , Ecosyst. Environ.* **2011**, 140, 164–173.
34. Jurado; Borges; Brouyère *Sci. Total Environ.* **2017**, 584–585, 207–218.
35. Olah; Goepfert; Prakash *Beyond oil and gas : the methanol economy*; Wiley-VCH: Weinheim, Germany, 2018; .
36. Nam *Acc. Chem. Res.* **2007**, 40, 522–531.
37. Matsunaga; Mavropoulos; Hillhouse *Polyhedron* **1995**, 14, 175–185.
38. Prince; Gunnoe; Cundari *Dalton Trans.* **2014**, 43, 7608–7614.
39. Mei; Carsch; Freitag; Gunnoe; Cundari *J. Am. Chem. Soc.* **2013**, 135, 424–435.
40. Matsunaga; Hillhouse; Rheingold *J. Am. Chem. Soc.* **1993**, 115, 2075–2077.
41. Burch; Daniells; Breen; Hu A combined transient and computational study of the dissociation of N₂O on platinum catalysts. **2004**, 224, 252–260.
42. Martínez; Goursot; Coq; Delahay *J Phys Chem B* **2004**, 108, 8823–8829.
43. Dibeler *J. Chem. Phys.* **1967**, 47, 2191–2192.
44. Danopoulos; Pugh; Smith; Saßmannshausen *Chemistry : a European journal* **2009**, 15, 5491–5502.
45. Darmon; Yu; Semproni; Turner; Stieber; DeBeer; Chirik *Organometallics* **2014**, 33, 5423–5433.
46. Scott; Stevens; Dorta; Costabile; Cavallo; Hoff; Nolan Steric and Electronic Properties of N-Heterocyclic Carbenes (NHC): A Detailed Study on Their Interaction with Ni(CO)₄. **2005**, 127, 2485–2495.
47. Rosen; Varnado; Tennyson; Khramov; Kamplain; Sung; Cresswell; Lynch; Bielawski *Organometallics* **2009**, 28, 6695–6706.
48. Peñrez; Díaz-Requejo; Nolan *N-Heterocyclic Carbenes in Synthesis*; 2006; .
49. Muehlhofer; Strassner; Herrmann *Angew. Chem. Int. Ed.* **2002**, 41, 1745–1747.
50. Kiernicki; Zeller; Szymczak *Inorg. Chem.* **2019**, 58, 1147–1154.

51. Zimmer; Burkhardt; Friedrich; Steube; Neuba; Schepper; Müller; Flörke; Huber; Lochbrunner; Bauer *Inorg. Chem.* **2018**, *57*, 360–373.
52. Danopoulos; Wright; Motherwell; Ellwood *Organometallics* **2004**, *23*, 4807.
53. Arduengo; Gamper; Calabrese; Davidson *J. Am. Chem. Soc.* **1994**, *116*, 4391–4394.
54. Arduengo Looking for Stable Carbenes: The Difficulty in Starting Anew. **1999**, *32*, 913–921.
55. Arduengo; Harlow; Kline *J. Am. Chem. Soc.* **1991**, *113*, 361–363.
56. Zimmer; Müller; Burkhardt; Schepper; Neuba; Steube; Dietrich; Flörke; Mangold; Gerhards *Eur. J. Inorg. Chem.* **2017**, *2017*, 1504.
57. Danopoulos; Simler; Braunstein *Chem. Rev.* **2019**, *119*, 3730–3961.
58. Dröge; Glorius *Angewandte Chemie International Edition* **2010**, *49*, 6940–6952.
59. Dalton; Faber; Glorius *ACS Cent. Sci.* **2021**, *7*, 245–261.
60. Groves *J. Inorg. Biochem.* **2006**, *100*, 434–447.
61. Moody; Raven *Acc. Chem. Res.* **2018**, *51*, 427–435.
62. Que; Tolman *Nature* **2008**, *455*, 333–340.
63. McDonald; Que *Coord. Chem. Rev.* **2013**, *257*, 414–428.
64. Krebs; Galonić Fujimori; Walsh; Bollinger *Acc. Chem. Res.* **2007**, *40*, 484–492.
65. Wang; Olankitwanit; Rajca; Rajca *J. Am. Chem. Soc.* **2017**, *139*, 7144–7147.
66. Valgimigli; Banks; Ingold; Lusztyk *J. Am. Chem. Soc.* **1995**, *117*, 9966–9971.
67. Seal; Oyedepo; Truhlar *J Phys Chem A* **2013**, *117*, 275.
68. Renaud; Beaufile; Feray; Schenk *Angewandte Chemie International Edition* **2003**, *42*, 4230–4233.
69. Neidig; Decker; Choroba; Huang; Kavana; Moran; Spencer; Solomon *Proceedings of the National Academy of Sciences* **2006**, *103*, 12966.
70. Mayer *Acc. Chem. Res.* **1998**, *31*, 441–450.
71. Mai; Kim *Inorg. Chem.* **2016**, *55*, 3844–3852.
72. Shubin; Ruzankin; Zilberberg; Parmon Distinct activity of the oxyl FeIII O group in the methane dissociation by activated iron hydroxide: DFT predictions. **2015**, *640*, 94–100.
73. Dietl; Schlangen; Schwarz *Angewandte Chemie International Edition* **2012**, *51*, 5544–5555.
74. Pan; Wenger; Matthews; Pollock; Bhardwaj; Kim; Allen; Grossman; Krebs; Bollinger *J. Am. Chem. Soc.* **2019**, *141*, 15153–15165.
75. Simons; Prinslow; Babucci; Hoffman; Hong; Vitillo; Bare; Gates; Lu; Gagliardi; Bhan *J. Am. Chem. Soc.* **2021**, *143*, 12165–12174.
76. Bach *J Phys Chem A* **2016**, *120*, 840–850.
77. American Chemical Society. Division of Inorganic Chemistry.; American Chemical Society. Meeting 2002 : Orlando, Fla.); Goldberg; Goldman *Activation and functionalization of C-H bonds*; American Chemical Society: Washington, District of Columbia, 2004; .
78. Frisch; Trucks; Schlegel; Scuseria; Robb; Cheeseman; Scalmani; Barone; Petersson; Nakatsuji; Li; Caricato; Marenich; Bloino; Janesko; Gomperts; Mennucci; Hratchian; Ortiz; Izmaylov; Sonnenberg; Williams-Young; Ding; Lipparini; Egidi; Goings; Peng; Petrone; Henderson; Ranasinghe; Zakrzewski; Gao; Rega; Zheng; Liang; Hada; Ehara; Toyota; Fukuda; Hasegawa; Ishida; Nakajima; Honda; Kitao; Nakai; Vreven; Throssell; Montgomery; Peralta; Ogliaro; Bearpark; Heyd; Brothers; Kudin; Staroverov; Keith; Kobayashi; Normand; Raghavachari; Rendell; Burant; Iyengar; Tomasi; Cossi; Millam; Klene; Adamo; Cammi; Ochterski; Martin; Morokuma; Farkas; Foresman; Fox *GAUSSIAN 16. Revision C.01*; Gaussian Inc., Wallingford, CT, 2016.

79. Austin; Petersson; Frisch; Dobek; Scalmani; Throssell *J. Chem. Theory Comput.* **2012**, *8*, 4989–5007.
80. Stevens; Krauss; Basch; Jasien *Can. J. Chem.* **1992**, *70*, 612–630.
81. Becke *J. Chem. Phys.* **1993**, *98*, 5648–5652.
82. Lee; Yang; Parr *Phys. Rev. B* **1988**, *37*, 785–789.
83. Stevens; Krauss; Basch; Jasien *Can. J. Chem.* **1992**, *70*, 612–630.
84. Zhao; Truhlar *Theor. Chem. Acc.* **2008**, *120*, 215.
85. Austin; Petersson; Frisch; Dobek; Scalmani; Throssell; J Chem A Density Functional with Spherical Atom Dispersion Terms.
86. Bosch; Moreno; Lluch; Bertrán *Chem. Phys. Lett.* **1989**, *160*, 543–548.
87. Coskun; Jerome; Friesner *J. Chem. Theory Comput.* **2016**, *12*, 1121–1128.
88. Austin; Petersson; Frisch; Dobek; Scalmani; Throssell *Journal of chemical theory and computation* **2012**, *8*, 4989–5007.
89. Marenich; Cramer; Truhlar *J Phys Chem B* **2009**, *113*, 6378–6396.
90. A New Basis Set Exchange: An Open, Up-to-date Resource for the Molecular Sciences Community; The role of databases in support of computational chemistry calculations; Basis Set Exchange: A Community Database for Computational Sciences; Balanced basis sets of split valence, triple zeta valence and quadruple zeta valence quality for H to Rn: Design and assessment of accuracy. , 4814–1052; 3297.
91. Schmidt; Gordon; Dupuis *J. Am. Chem. Soc.* **1985**, *107*, 2585–2589.
92. Santini; Marinelli; Pelli *European journal of inorganic chemistry* **2016**, *2016*, 2312–2331.
93. Groom, C. et al. Cambridge Structural Database the Cambridge Structural Databases. **2021**, ConQuest Version 2.0.1; 12 Union Road, Cambridge, CB2 1EZ, UK.
94. Wurzenberger; Piotrowski; Klüfers *Angew. Chem. Int. Ed.* **2011**, *50*, 4974–4978.
95. Cao; Nørskov *ACS Catal.* **2023**, *13*, 3456–3462.
96. Press Understanding the effect of catalyst spin state on reaction. <https://phys.org/news/2024-01-effect-catalyst-state-reaction.html> (accessed Dec 16, 2024).
97. Prince; Cundari; Tymczak *J Phys Chem A* **2014**, *118*, 11056–11061.

Disclaimer/Publisher's Note: The statements, opinions and data contained in all publications are solely those of the individual author(s) and contributor(s) and not of MDPI and/or the editor(s). MDPI and/or the editor(s) disclaim responsibility for any injury to people or property resulting from any ideas, methods, instructions or products referred to in the content.